Fast Li-Ion Insertion into Nanosized $LiMn_2O_4$ without Domain Boundaries

Masashi Okubo,[†] Yoshifumi Mizuno,[†] Hirotoshi Yamada,[‡] Jedeok Kim,[§] Eiji Hosono,[†] Haoshen Zhou,[†] Tetsuichi Kudo,[†] and Itaru Honma[†,*]

[†]National Institute of Advanced Industrial Science and Technology (AIST), Umezono 1-1-1, Tsukuba, Ibaraki, 305-8578 Japan, [‡]Faculty of Engineering, Nagasaki University, Graduate School of Science and Technology, Nagasaki University, Bunkyo 1-14, Nagasaki, 852-8521 Japan, and [§]National Institute for Materials Science (NIMS), Tsukuba, Ibaraki,305-0044 Japan

ABSTRACT The effect of crystallite size on Li-ion insertion in electrode materials is of great interest recently because of the need for nanoelectrodes in higher-power Li-ion rechargeable batteries. We present a systematic study of the effect of size on the electrochemical properties of $LiMn_2O_4$. Accurate size control of nanocrystalline $LiMn_2O_4$, which is realized by a hydrothermal method, significantly alters the phase diagram as well as Li-ion insertion voltage. Nanocrystalline $LiMn_2O_4$ with extremely small crystallite size of 15 nm cannot accommodate domain boundaries between Li-rich and Li-poor phases due to interface energy, and therefore lithiation proceeds *via* solid solution state without domain boundaries, enabling fast Li-ion insertion during the entire discharge process.

KEYWORDS: Li-ion rechargeable battery · cathode · $LiMn_2O_4$ · nanosize effect · domain boundary

Li-ion batteries have been intensively investigated for use in high-power applications such as electric vehicles, plug-in hybrid electric vehicles, and hybrid electric vehicles.[1,2] However, in spite of the efficiency, lightweight, and high energy density of Li-ion batteries, all of which are appropriate for portable electric devices, their power density remains too low for such applications.

A serious problem with low power density is possible large polarization in electrolyte and solid electrodes. In particular, slow Li-ion diffusion in cathode materials results in insufficient Li-ion insertion/extraction under high charge/discharge rate conditions.[3] Therefore, reduction of crystallite size of cathode materials could enhance high charge/discharge rate capability due to their short Li-ion diffusion length.[4,5]

However, a large surface in nanosized cathode materials may also affect structural, physical, and electrochemical properties.[6,7] For example, the surface energy in anatase Li_xTiO_2 and olivine Li_xFePO_4 is reported to decrease the miscibility gap and stabilize a solid solution state.[8−11] We recently reported that, as crystallite size of Li_xCoO_2 decreases below 30 nm, spatial distribution of the energy required for Li-ion insertion gives unusual charge/discharge curves.[12]

In this paper, we focus on the effect of nanosize on $Li_xMn_2O_4$. These spinel-type materials are promising candidates to replace $LiCoO_2$ layered-type materials used widely for current commercial Li-ion batteries. As a stable phase at room temperature, $LiMn_2O_4$ (which corresponds to $x = 1$ in $Li_xMn_2O_4$) has a cubic spinel structure (space group *Fdm*) with Li-ion in a tetrahedral 8*a* site and Mn-ion in an octahedral 16*d* site.[13] When Li-ion is extracted electrochemically from $LiMn_2O_4$, $Li_xMn_2O_4$ solid solution with the cubic spinel structure is formed for $0.35 < x < 1$.[14,15] In contrast, when Li-ion is inserted electrochemically into $LiMn_2O_4$, it intercalates into another octahedral 16*c* site to form a cubic spinel phase with higher Li-ion concentration ($[Li]_2^{16c}[Mn]_2^{16d}O_4$), which immediately relaxes to a tetragonal spinel phase due to the Jahn−Teller distortion ($[Li]_2^{8d}[Mn]_2^{8c}O_4$, $I4_1/amd$).[16−19]

Phase transformation from cubic spinel to tetragonal spinel is accompanied by a large unit cell expansion, because the axial Mn−O distance elongates from 1.96 to 2.29 Å.[13,20] Therefore, Li-ion insertion for $1 < x < 2$ proceeds not *via* solid solution, but by fractional change of two phases. As a consequence, when crystallite size is considerably large, full lithiation throughout the particle cannot be achieved due to slow movement of the domain boundaries.

In contrast to the compound with large crystallite size, nanosized $LiMn_2O_4$, prepared by various methods including sol−gel method,[21−23] ball-milling,[24] templating,[25] ultrasonic spray pyrolysis,[26] and

*Address correspondence to i.homma@aist.go.jp.

Received for review September 10, 2009 and accepted January 22, 2010.

Published online January 29, 2010.
10.1021/nn9012065

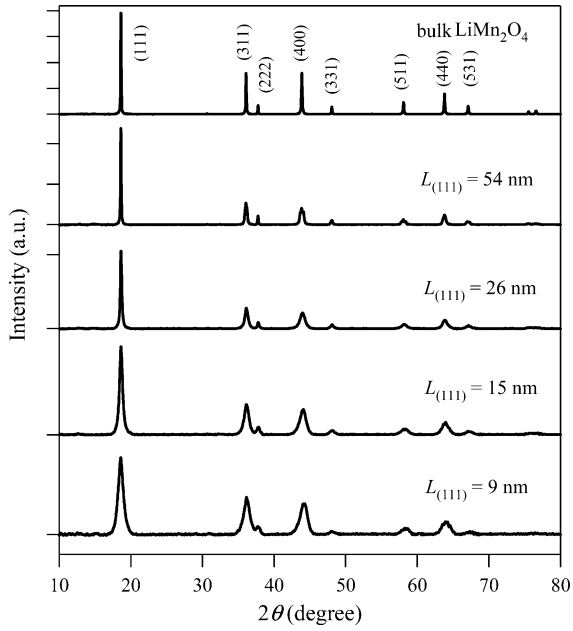

Figure 1. Powder XRD patterns for nanocrystalline $LiMn_2O_4$ synthesized by hydrothermal reaction. The pattern for bulk $LiMn_2O_4$ is shown for comparison.

other techniques,[27,28] has been reported to show complete Li-ion insertion/extraction for $1 < x < 2$. Although surface and interface energy are expected to play crucial roles in this nanosize effect, a systematic analysis with precisely size-controlled $LiMn_2O_4$ has not been performed.

The effect of crystallite size on material properties is generally due to several factors acting simultaneously, such as absence of long-range cooperative interactions, structural defects, and elastic constraints. For example, with decreasing crystallite size, long-range cooperative interaction for the development of a new phase decreases too much to drive the transition.[29] It is also well-known that hydroxyl ions can reside as defects on oxygen sites within nanocrystalline transition-metal oxides, and so can upset the phase transition.[30] Other factors can also come into play. Therefore, attempts to identify a general critical size of $LiMn_2O_4$ for electrochemical use, or a single cause for all nanosize effects on $LiMn_2O_4$ are unrealistic.

Here we report a systematic study of the effect of nanosize on the electrochemical properties of $LiMn_2O_4$. Formation of domain boundaries in $LiMn_2O_4$, which prevents complete Li-ion insertion/extraction for $1 < x < 2$ in bulk $Li_xMn_2O_4$, is suppressed as crystallite size decreases. Without domain boundaries, nanocrystalline $LiMn_2O_4$ with crystallite size of 15 nm exhibits full capacity at such a high discharge rate of 10 C (2.98 A/g).

RESULTS AND DISCUSSION

Nanocrystalline $LiMn_2O_4$ was synthesized by hydrothermal reaction of nanosized orthorhombic $LiMnO_2$ (*o*-$LiMnO_2$),[31] LiOH, and H_2O. Nanosized *o*-$LiMnO_2$ was synthesized by *in situ* oxidation-ion exchange method reported in the literature.[32] TEM images (Figure S1, Supporting Information) shows that the nanosized *o*-$LiMnO_2$ has extremely thin nanoplatelet morphology. The extremely small crystallite size of the precursor contributes to immediate dissolution into aqueous solution, and immediate formation of a $LiMn_2O_4$ phase under hydrothermal conditions.

The crystallite size of nanocrystalline $LiMn_2O_4$ was controlled by varying the amount of LiOH, reaction temperature, and reaction time. Figure 1 shows powder XRD patterns for the resulting compounds. The pattern for bulk $LiMn_2O_4$ is shown for comparison. The experimental conditions for each compound are listed in Table 1. All peaks correspond to $LiMn_2O_4$ (*Fdm*),[13] indicating that the hydrothermal reaction gives $LiMn_2O_4$ without any impurity phase. Peak line width broadens at lower reaction temperature, shorter reaction time, and higher LiOH concentration. This tendency is similar to that for the previously reported hydrothermal synthesis of nanocrystalline $LiCoO_2$.[12] The crystallite size, estimated from the (111) peak ($L_{(111)}$) by the Scherrer equation, varies from 9 to 54 nm.

Figure 2 panels a and b show TEM images for $LiMn_2O_4$ with $L_{(111)} = 9$ and 54 nm, respectively. Extremely small nanoparticles with crystallite size of about 10 nm are visible for the compound with $L_{(111)} = 9$ nm; large particles with crystallite size of a few hundred nanometers are visible for the compound with $L_{(111)} = 54$ nm. Images for the compounds with $L_{(111)} = 15$ and 26 nm are shown in Figure S2 (Supporting Information). The figures shows that crystallite size decreases as $L_{(111)}$ decreases.

To confirm the size-controlled synthesis of $LiMn_2O_4$, we determined the distribution of particle size from the TEM images for each compound (Figure 2c). It is clear that size distribution is controlled by the hydrothermal reaction. The mean particle size *L* observed in the TEM images is also noted in the figure. Although the observed values of *L* are slightly larger than $L_{(111)}$, *L* decreases with decreasing $L_{(111)}$. Furthermore, the BET sur-

TABLE 1. Synthetic Conditions and Characterization of Obtained Products

reaction temp (°C)	reaction time (h)	[LiOH] (mM)	$L_{(111)}$ (nm)	*L* (nm)	BET surface area (m^2/g)	*a* (Å)	*V* (Å^3)	Mn valence	Li/Mn ratio (ICP)	stoichiometry
180	12	10	9	15	38.7	8.219(6)	555(1)	+3.52(7)	0.425	$Li_{0.85}Mn_2O_{3.75}(OH)_{0.35}$
200	72	10	15	20	28.7	8.229(3)	557.3(6)	+3.48(2)	0.465	$Li_{0.93}Mn_2O_{3.83}(OH)_{0.27}$
200	168	10	26	43	18.8	8.237(1)	558.9(2)	+3.51(13)	0.49	$Li_{0.98}Mn_2O_{3.98}(OH)_{0.02}$
200	168	0	54	210	13.2	8.2466(3)	560.82(6)	+3.48(1)	0.475	$Li_{0.95}Mn_2O_{3.99}(OH)_{0.01}$

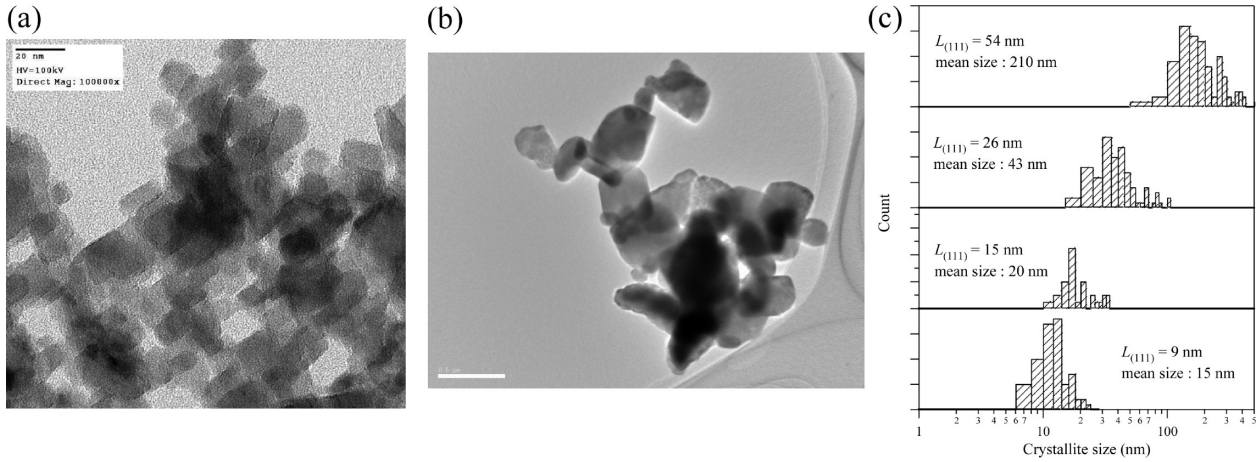

Figure 2. (a b) TEM images of nanocrystalline $LiMn_2O_4$ with $L_{(111)}$ = 9 and 54 nm, respectively; a black bar is 20 nm and a white bar is 500 nm; (c) distribution of crystallite size for nanocrystalline $LiMn_2O_4$ counted from the TEM images; the mean particle size is also noted.

face area monotonically increases with decreasing $L_{(111)}$ as shown in Table 1. All these results support the size-controlled synthesis of nanocrystalline $LiMn_2O_4$ by the hydrothermal reaction. Hereafter, for simplicity, we use the mean particle size L observed in the TEM images as "crystallite size" of nanocrystalline $LiMn_2O_4$.

In general, from a structural viewpoint, $LiMn_2O_4$ has many possible nonstoichiometries and structural defects such as cationic disorder and oxygen deficiency.[33] For example, the Li-ion can occupy the octahedral 16*d* site by substituting for the Mn-ion ($Li^{8a}[Li_xMn_{2-x}]^{16d}O_4$).[34] Oxygen deficiency can also occur by substitution of one O atom at the irregular 8*b* site for two O atoms at the regular 32*e* site.[35] Furthermore, structural features near the surface should differ significantly from those at the inner core. For example, hydroxyl ions frequently reside as defects on O sites within transition-metal oxides, especially near the surface.[30]

However, X-ray diffraction relies on coherent scattering from the spatial average of a large number of unit cells. It is, therefore, insensitive to subtle structural features or symmetry changes. Therefore, the XRD pattern measures only the global structure of nanocrystalline $LiMn_2O_4$. To probe the local structure of nanocrystalline $LiMn_2O_4$, other techniques are indispensable. In an attempt to characterize the local structural properties of nanocrystalline $LiMn_2O_4$, we used a combination of XAS, ICP-AES, and IR spectroscopy.

Figure 3a shows Mn K-edge X-ray absorption near edge structure (XANES) for nanocrystalline $LiMn_2O_4$. The spectrum for bulk $LiMn_2O_4$ is also shown for comparison. Each spectrum shows weak pre-edge features

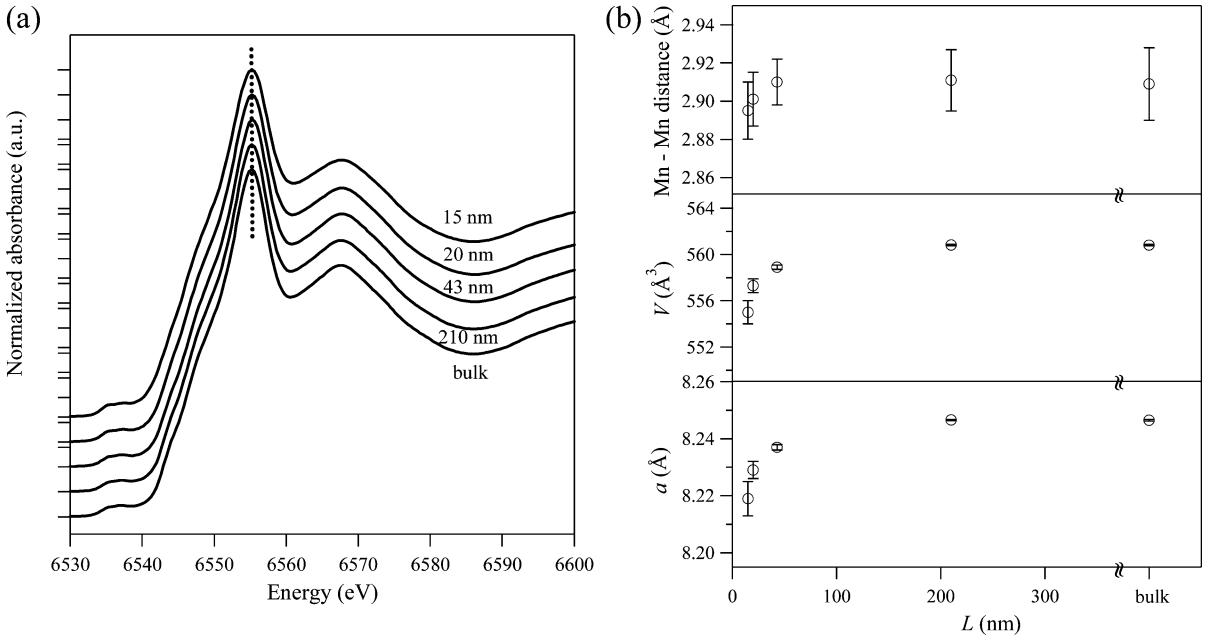

Figure 3. (a) Mn K-edge XANES spectra for bulk and nanocrystalline $LiMn_2O_4$; (b) unit cell parameters from the powder XRD pattern and Mn−Mn interatomic distance from EXAFS for nanocrystalline $LiMn_2O_4$.

from 6535 to 6540 eV, ascribed to excitation from 1s to 3d orbitals. The main absorption peak at about 6555 eV arises from the Laporte-allowed transition from 1s to 4p orbitals.[36−38] It is well-known that the main peak position of the Mn K-edge is sensitive to the valence state of the Mn-ion. The peak generally shifts to lower energy when the valence state is reduced and shifts to higher energy when the valence state is increased.[36] As shown in the figure, the position of the main peak for all compounds is almost the same as that for bulk $LiMn_2O_4$, so the averaged valence state of the Mn-ion in nanocrystalline $LiMn_2O_4$ can be estimated to be +3.5. In fact, the averaged valence states of the Mn-ion determined by a procedure described by Wickham[39] are +3.52, +3.48, +3.51, and +3.48 for L = 15, 20, 43, and 210 nm, respectively.

In contrast, ICP measurements indicate nonstoichiometry in nanocrystalline $LiMn_2O_4$. Li/Mn ratios for nanocrystalline $LiMn_2O_4$ (0.5 for ideal stoichiometry) are 0.425, 0.465, 0.49, and 0.475 for L = 15, 20, 43, and 210 nm, respectively. Thus, with decreasing crystallite size, the Li-ion content decreases, although the valence state of the Mn-ion remains constant.

To explain these results, we suggest that the O atoms, especially near the surface, may be deficient or substituted by hydroxyl ions. Indeed, IR spectra confirm the existence of hydroxyl ions, as the stretching mode of O−H is clearly observed at about 3400 cm^{-1} (Figure S3, Supporting Information). This broad absorption band agrees well with previously reported experimental[40] and calculated vibration frequencies for the protonized manganese spinel.[41] Thus, the stoichiometry of nanocrystalline $LiMn_2O_4$ can be described as $Li_{0.85}Mn_2O_{4-z}(OH)_{2z-0.15}$ (L = 15 nm), $Li_{0.93}Mn_2O_{4-z}(OH)_{2z-0.07}$ (L = 20 nm), $Li_{0.98}Mn_2O_{4-z}(OH)_{2z-0.02}$ (L = 43 nm), and $Li_{0.95}Mn_2O_{4-z}(OH)_{2z-0.05}$ (L = 210 nm). The value of z deduced from the ICP results is 0.25 (L = 15 nm), 0.17 (L = 20 nm), 0.02 (L = 43 nm), and 0.01 (L = 0.01). However, it should be noted that the above stoichiometry is only an averaged stoichiometry over the assembly of nanoparticles. The composition within a particle is not homogeneous and may depend on the distance from the surface.

To investigate further the structural properties of nanocrystalline $LiMn_2O_4$, we conducted extended X-ray absorption fine structure (EXAFS) spectroscopy (Figure S4, Supporting Information). The experimental spectrum $\chi(k)$ was fitted with the two simple diffusion paths for Mn−O and Mn−Mn, and coordination numbers were fixed at 6 for both pairs. Simple single-scattering calculation satisfactorily reproduced the experimental spectrum. Figure 3b shows the determined Mn−Mn interatomic distance plotted as a function of crystallite size. The distance decreases as the crystallite size decreases. This tendency is confirmed by unit cell parameters calculated from the powder XRD pattern and shown in the same figure. The parameters were calculated by least-squares fitting with the peak-top values in the pattern. With decreasing crystallite size, a and V decrease in accordance with the tendency of the Mn−Mn interatomic distance. The decrease in unit cell parameters for $LiMn_2O_4$ is frequently ascribed to substitution for the Mn-ion by the Li-ion ($Li^{8a}[Li_xMn_{2-x}]^{16d}O_4$). However, the Li/Mn ratio determined by the ICP is clearly inconsistent with Li-excess stoichiometry. It is most likely that the O atom near the surface deviates from the regular 32e site due to structural defects such as hydroxyl ions and O deficiencies, which decreases lattice parameters. The structural disorders of the O atom should also give the Mn−O distance change, but the simple scattering calculation cannot clearly determine the distance change.

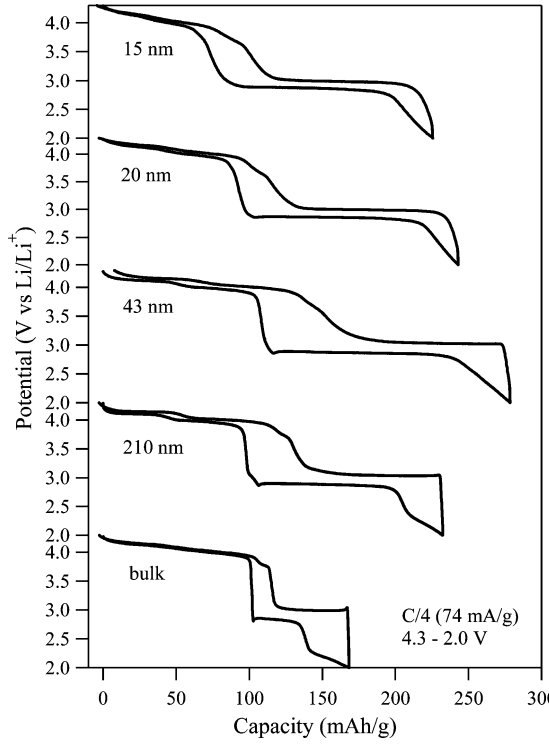

Figure 4. Charge−discharge curves for bulk and nanocrystalline $LiMn_2O_4$ at a constant charge/discharge rate of C/4 (74 mA/g) between 4.3 and 2.0 V.

The above discussion suggests that nanocrystalline $LiMn_2O_4$ with controlled crystallite size from 15 to 210 nm was successfully synthesized by the hydrothermal method. In the following discussion, we characterize the electrochemical properties of nanocrystalline $LiMn_2O_4$ and discuss the nanosize effect.

Figure 4 shows the charge (Li-ion extraction)/discharge (Li-ion insertion) curve for nanocrystalline $LiMn_2O_4$, obtained after first charging to 4.3 V. The curve for bulk $LiMn_2O_4$ is also shown for comparison. The charge/discharge rate was C/4 (74 mA/g); cut off voltages were 4.3 and 2.0 V. All of the compounds show a charge/discharge capacity at about 4 V ($x < 1$) and 3 V ($x > 1$ in $Li_xMn_2O_4$), and Li-ions are reversibly inserted and extracted. Bulk $LiMn_2O_4$ shows discharge capacities

of 102 mAh/g at 4 V, corresponding to $0.3 < x < 1$, but only 66 mAh/g at 3 V, corresponding to $1 < x < 1.45$.

In contrast, for nanocrystalline $LiMn_2O_4$ with crystallite size $L = 43$ nm, the Li-ion successfully intercalates into the host to show discharge capacities of 111 mAh/g at 4 V ($0.25 < x < 1$) and 166 mAh/g at 3 V ($1 < x < 2.1$). However, capacity decreases with further nanosizing below 43 nm. Nanocrystalline $LiMn_2O_4$ with crystallite size $L = 15$ nm shows discharge capacity of 140 mAh/g at 3 V ($1 < x < 1.95$), but only 85 mAh/g at 4 V ($0.42 < x < 1$). For simplicity, we assumed the composition at 3.3 V (*vs* Li/Li^+) to be $x = 1$, and calculated the value of x during the charge−discharge process assuming the host material to be $Li_xMn_2O_4$, although nonstoichiometry was observed.

To analyze more precisely the effect of nanosize on the electrochemical properties of $LiMn_2O_4$, we recorded the open-circuit voltage (OCV) curve by the galvanostatic intermittent titration technique (GITT), with repeated cycles of slow charge/discharge rate of C/8 (37 mA/g) for 10 min followed by interruption for 10 min. Figure 5 shows the obtained OCV curves for selected compounds. Solid lines are voltage changes during the experiment; circles are OCVs recorded after interruption. Although 10 min interruption seems insufficient to reach an equilibrium state, longer interruption results in nucleation of a new phase. This instability of manganese oxides has been reported frequently.[13] Therefore, interruption was kept constant at 10 min. OCV curves for all compounds are shown in Figure S5 (Supporting Information).

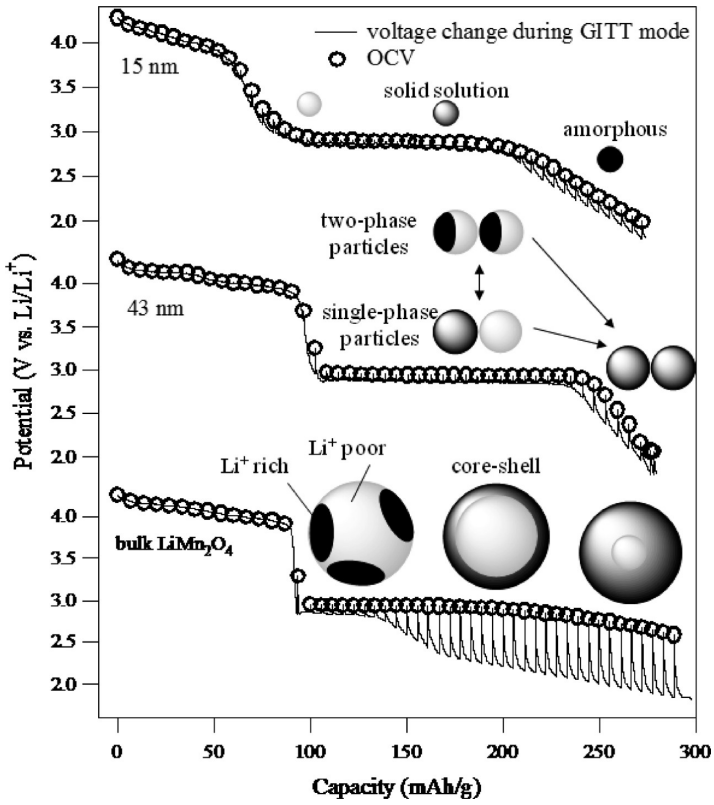

Figure 5. Open-circuit voltage (OCV) curves for bulk and nanocrystalline $LiMn_2O_4$. Solid lines are voltage changes during the GITT experiment; circles are OCVs recorded after interruption for 10 min to reach equilibrium. Insets illustrate the lithiation process; dark areas are Li^+ rich and light areas are Li^+ poor. Note that lithiation for the compound with $L = 15$ nm proceeds without domain boundaries.

Consider first the effect of nanosize on charge/discharge capacity above 3.3 V, where the Li-ion at the regular octahedral 8*a* site is inserted/extracted. With decreasing crystallite size, capacity decreases above 3.9 V and increases below 3.9 V (Figure 5 and Supporting Information, Figure S6). This trend is similar to that for nanocrystalline $LiCoO_2$, as we reported previously.[12] Because the electric double layer capacity is small enough to be neglected on the basis of the BET surface area, this behavior can be explained by the spatial distribution of Li-site energy μ_{Li}^0 near the surface. μ_{Li}^0 is defined as the enthalpy change from inserting a Li-ion and an electron into the lattice.[42] The relationship between Li-site energy and Li chemical potential μ_{Li} for $Li_xMn_2O_4$ in the spherical space coordinate ($0 < r < L/2$) is[6]

$$\mu_{Li}(x) = \mu_{Li}^0(r) + kT \ln a_{Li}(r, x)$$

where $a_{Li}(r, x)$ is the activity of Li as a function of r and x. Note that the Li chemical potential is spatially uniform because the gradient of Li activity compensates for the spatially distributed μ_{Li}^0.

The spatial distribution of $\mu_{Li}^0(r)$ near the surface can be explained by electrostatic interaction change due to the finite lattice. Other possible explanations include the above-mentioned oxygen deficiency, hydroxyl ions, and structural disorder near the surface such as by cation mixing between Mn- and Li-ions. However, compared to previously reported nanocrystalline $LiCoO_2$ in which a surface layer of 3 nm was observed,[12] the surface effect of Li-ion insertion/extraction for $0 < x < 1$ is not large, because the analysis based on the lattice-gas model[43−45] indicates the specific surface of 1 nm thickness (Figure S6, Supporting Information).

In the following section, we consider the effect of nanosize on Li-ion insertion/extraction for $1 < x < 2$. Even for a low constant charge/discharge rate of C/4 (74 mA/g), sufficient Li-ion insertion/extraction cannot be achieved for bulk $LiMn_2O_4$ (Figure 4). Although it appears that the GITT mode for bulk $Li_xMn_2O_4$ can achieve lithiation up to $x \approx 2$ (Figure 5), the Li-ion insertion voltage (solid line in Figure 5) is much lower than the OCV, especially for the highly lithiated compounds. This strongly suggests that the tetragonal spinel phase covers the entire surface because of the small surface area. In general, a "core-shell" configuration is not preferred because of the influence of anisotropic structure or Li-

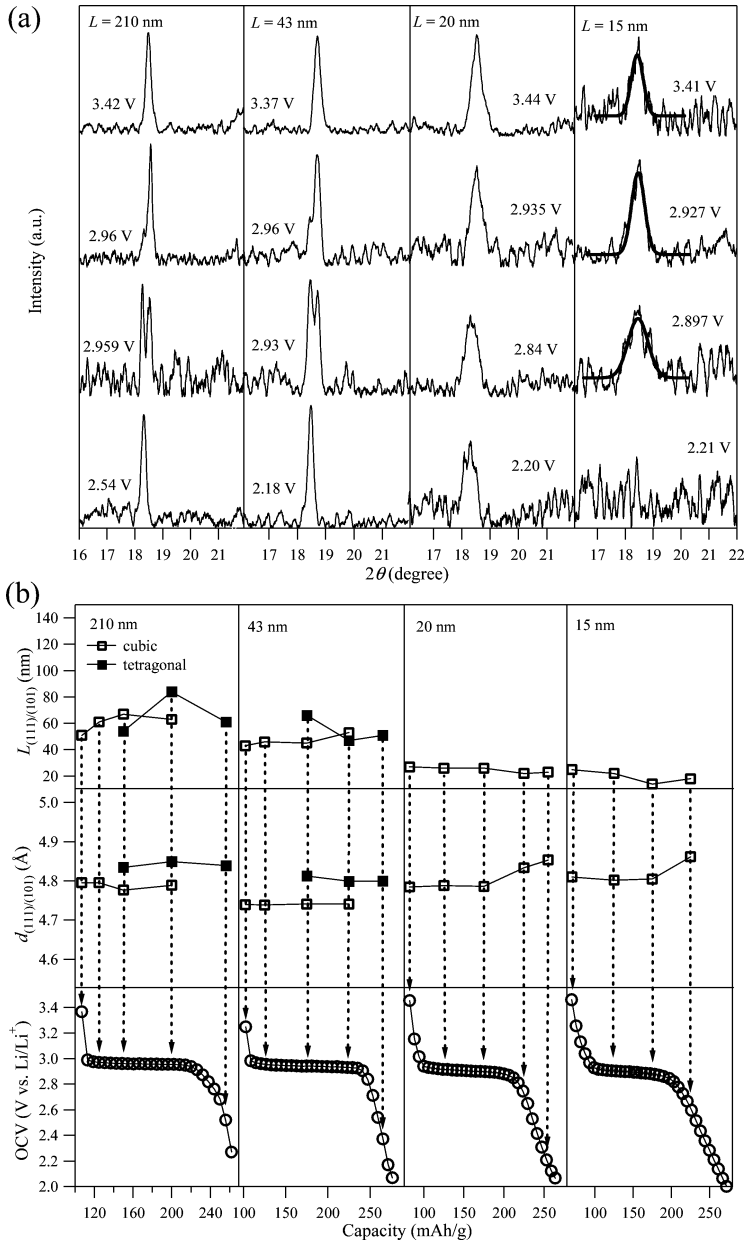

Figure 6. (a) *Ex situ* powder XRD patterns for nanocrystalline $LiMn_2O_4$. Bold lines are fitted results based on a Gaussian line shape. (b) *d*-Spacing and crystallite size corresponding to the (111) reflection of the cubic spinel phase and the (101) reflection of the tetragonal spinel phase.

ion diffusion. However, $LiMn_2O_4$ has isotropic cubic structure and Li-ion diffusion path, which enables the core−shell configuration. When the entire surface is covered with the tetragonal spinel phase, Li-ion insertion should proceed only *via* lithiation of the tetragonal spinel phase at the surface:

$$\delta Li^+ + \delta e^- + [Li]_2^{8d}[Mn]_2^{8c}O_4 \rightarrow Li_\delta[Li]_2^{8d}[Mn]_2^{8c}O_4$$

Because lithiation of the tetragonal spinel phase at the surface clearly requires a lower voltage than does lithiation of the cubic spinel phase because of reduction from Mn^{3+} to Mn^{2+}, the large polarization for bulk $LiMn_2O_4$ evidence that the surface is completely covered with the tetragonal spinel phase. The large polarization is also recorded for the compound with $L = 210$ nm (Figure S5).

When nanoparticle size is reduced to 43 nm, the large polarization at the region of high Li-ion concentration almost disappears (Figure 5). The large surface area of nanoparticles smaller than 43 nm should prevent them from being completely covered with the tetragonal spinel phase. Suppression of large polarization can explain the complete Li-ion insertion/extraction for $1 < x < 2$ under the constant charge/discharge rate of C/4 below crystallite size of 43 nm (Figure 4).

Further nanosizing below 43 nm results in the decrease in the capacity at the plateau region and the increase in the capacity below the plateau region. This can be explained by the extension of the solid solution limit of the lithiated phase ($Li_{2-\beta}Mn_2O_4$) due to the surface energy.

Nanosizing $LiMn_2O_4$ also affects the OCV at the two-phase region. Previously, Jamnik *et al.* expected that, for particles smaller than 100 nm, electrochemical properties are generally affected by surface energy.[46] Wagemaker *et al.* stressed the importance of the interface energy of domain boundaries as well as the surface energy.[47] Apparently, for nanocrystalline $LiMn_2O_4$, the effect of nanosize on the Li chemical potential is not simple, but includes effects from structural disorder such as hydroxyl ions. Nevertheless, as crystallite size decreases, the average OCV value at the plateau region decreases from 2.97 to 2.90 V (Figure S6a, Supporting Information). The dependence of OCV on crystallite size suggests the influence of surface and interface energies, although structural disorder is also important.

In further investigating the influence of surface and interface energies, nanosized Li_xTiO_2 particles smaller than 120 nm are reported to consist of either the anatase or the Li-titanate phase, to suppress the additional molar Gibbs free energy of domain boundaries.[8] A mixture of single-phase particles forms after initial formation of metastable two-phase particles containing domain boundaries.[9−11] Thus, for $LiMn_2O_4$, a mixture of single-phase particles could similarly form with nanosizing.

Figure 6a shows the (111) reflection in the *ex situ* XRD patterns during discharge for each compound. Bold lines are fitted results based on a Gaussian line shape. For compounds with $L = 210$ and 43 nm, as lithiation proceeds, the (111) peak for the $LiMn_2O_4$ cubic spinel phase (*Fdm*) gradually disappears and the new (101) peak for the $Li_2Mn_2O_4$ tetragonal spinel phase ($I4_1/amd$) emerges. Figure 6b shows the *d*-spacing and crys-

tallite size estimated from the corresponding peak. Cubic and tetragonal spinel phases are clearly distinguished by the (111) and (101) peaks, and the *c*-axis is elongated due to the cooperative Jahn−Teller distortion of Mn^{III}-ions along that axis. However, crystallite size for each domain remains nearly constant during the entire lithiation process, which suggests the particles consist of either the cubic or tetragonal spinel phase.

In contrast, for the compounds with $L = 20$ and 15 nm, the (111) peak gradually shifts as lithiation proceeds. Although we cannot clearly distinguish between two phases, the *d*-spacing is also elongated. Again, the elongation can be attributed to the cooperative Jahn−Teller distortion of Mn^{III}-ions. This result suggests the disappearance of phase coexistence, and the lithiation *via* a solid solution over the whole compositional range. However, for the compound of $L = 20$ nm, the overpotential recorded just before entering the two-phase region under the constant discharge rate of C/4 indicates phase coexistence (Figure S6b, Supporting Information). Overpotential should relate to the additional free energy to form domain boundaries.[47] As shown in the figure, with decreasing crystallite size, overpotential becomes suppressed, but is still present for compounds with $L > 20$ nm. This indicates that metastable two-phase particles with domain boundaries initially form even for the compound with $L = 20$ nm, then transform to a mixture of single-phase particles.[11] Only the compound with $L = 15$ nm shows no overpotential, suggesting that lithiation may occur without formation of domain boundaries.

It was difficult to determine accurate lattice constants from the *ex situ* XRD pattern, because the other peaks are too weak to be recorded owing to broad line width and small amount of sample. Furthermore, for the compound with $L = 15$ nm, the (111) reflection grows too weak to be observed as lithiation proceeds. As pointed out by Meethong *et al.*,[11] the additional surface and interface energies by nanosizing may be relieved by formation of an amorphous phase. It is most likely that the compound with $L = 15$ nm also forms an amorphous phase, perhaps by distorting the Jahn−Teller Mn^{III}-ions along random orientations.

Disappearance of domain boundaries is also suggested by the transient current of the potentiostatic intermittent titration technique (PITT). Figure 7 shows the normalized transient current after an application of the potential step for the compound with $L = 43$, 20, and 15 nm. After the potential step from 2.9 to 2.85 V, the current for the compounds with $L = 43$ and 20 nm show the maximum value about 5 min later, while the current for the compound with $L = 15$ nm monotonously decreases. The maximum of the transient current for the large compounds suggests nucleation of the lithiated phase during the incubation time, thus proving the formation of domain boundaries. In contrast, the monotonous decrease in the current for the compound with $L = 15$ nm strongly supports disappearance of domain boundaries.

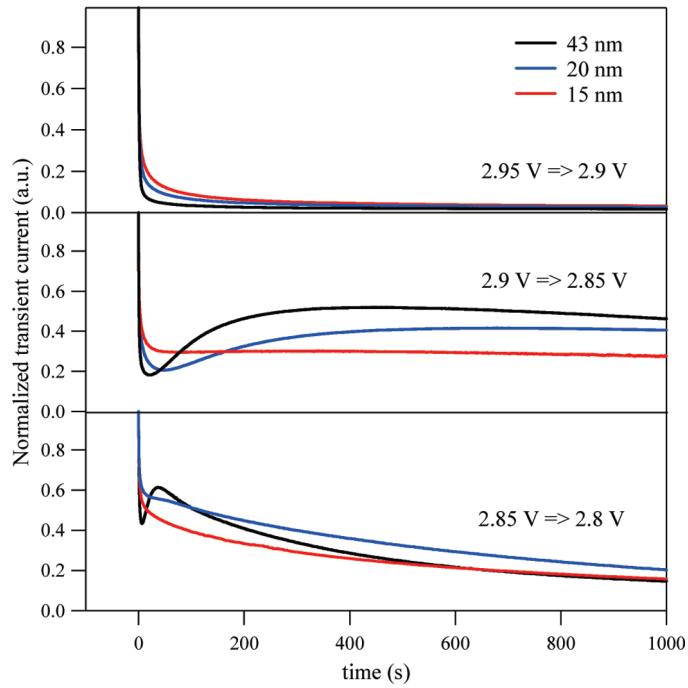

Figure 7. Transient current for nanocrystalline $LiMn_2O_4$ ($L = 43$, 20, and 15 nm) after application of the potential step of 50 mV.

To clarify the difference in lithiation processes more quantitatively, we analyzed the phase transformation kinetics based on the theory developed by Johnson, Mehl, and Avrami (the so-called JMA model).[48−51] In its basic form, the model describes the evolution of the volume fraction *f* with time *t* in terms of the nucleation frequency per unit volume *I* and the phase growth rate (that is, the moving speed of the domain boundaries) *u* as

$$f(t) = 1 - \exp[-g \int_0^t I(\int_t^t u\,dt)^m\,dt']$$

where *g* is a geometric factor that depends on the shape of the growing crystal and *m* is an integer or half integer that depends on the growth mechanism and the dimensionality of the crystal. Because the domain boundaries between the cubic and tetragonal phases should move along the *c*-axis (Figure 5), the equation becomes[49−51]

$$f(t) = 1 - \exp(-kt)$$

where *k* is the effective overall reaction rate containing the moving speed of the domain boundaries. Thus, the temperature dependence of *k* can provide the activation energy for the moving boundaries if the entire reaction is dominated by the moving boundaries. Application of the JMA model to $LiFePO_4$ gave the activation energy.[52]

To obtain the evolution of the volume fraction *f* with time *t* at various temperatures, we applied poten-

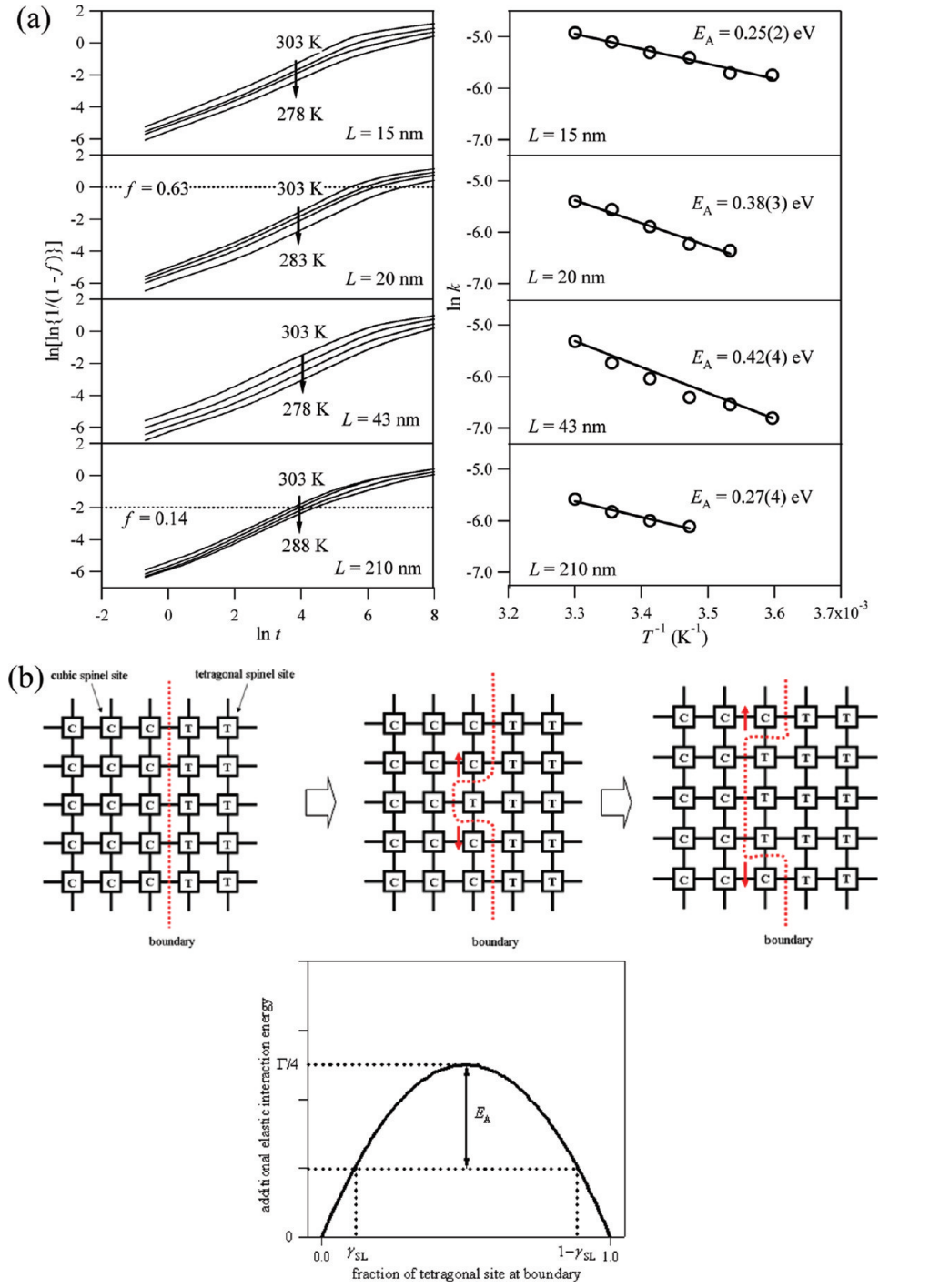

Figure 8. (a) Evolution of the tetragonal spinel phase volume fraction *f* with time *t* for nanocrystalline $LiMn_2O_4$ at various temperatures, and Arrhenius plot of the effective overall reaction rate *k*, where the solid line is the fitted result. (b) Schematic illustration of activation energy for the moving boundary between cubic- and tetragonal spinel phases. The generated kink glides apart transversely, and finally the entire boundary advances one periodic lattice.

tial in steps from 3.3 to 2.5 V [*vs* Li^+/Li] to the electrochemical cell in equilibrium in the temperature range 303−278 K, then recorded the resulting transient current until it became sufficiently small. With the application of this large potential step, the cubic phase should transform to the tetragonal phase. To avoid the dissolution of Mn-ions at high temperature and the crystallization of $LiClO_4$ from the electrolyte solution, the temperature was restricted to this range. The left side of Figure 8a shows the curves of $\ln[\ln(1/(1 - f(t)))]$ *vs* $\ln t$ at various temperatures for compounds with $L = 15$, 20, 43, and 210 nm. When the phase transformation obeys the above expression, the plot should have a slope of unity and an intercept of $\ln k$. As shown in the figure, the phase transformation from the cubic phase to the tetragonal phase proceeds by the potential step for all of the compounds, although time and temperature dependencies differ. The plot for the compound with $L =$

210 nm is linear curve and has a slope of unity over a short time range ($t < 60$ s). However, the plot deviates from the JMA model over a long-time range. The volume fraction of the tetragonal phase transformed in such a short time is only 0.14. This suggests that the basic assumption of the JMA model that the moving speed of the domain boundaries is a rate-limiting step during the entire lithiation process is no longer correct, because the compound with large crystallite size should be covered with the tetragonal phase immediately after the potential step and Li-ion diffusion should be prevented. In contrast, the plots for compounds with $L =$ 15, 20, and 43 nm obey the JMA model until 400 s, and the volume fraction of the tetragonal phase transformed in that time reaches to 0.63. Thus, we consider these three compounds further.

With decreasing temperature, the intercept of the plot (ln k) decreases for each compound. As mentioned above, k contains the moving speed of the domain boundaries, and the Arrhenius plot of k gives the activation energy for the moving boundaries if other factors are assumed temperature-independent. The right side of Figure 8a shows the Arrhenius plot of k for each compound. The activation energy for the moving boundaries obtained by least-squares fitting is also noted in the figure. For the compound with $L = 43$ nm, the activation energy is estimated to be 0.42 eV. Although the activation energy for Li-ion diffusion in $Li_{1+x}Mn_2O_4$ is unknown, this value is higher than the typical value for Li-ion diffusion in transition-metal oxides (roughly 0.2−0.3 eV).[53,54] Thus, the obtained value can be attributed to the activation energy for the moving boundaries.

Activation energy decreases with decreasing crystallite size. This can be explained by the extended solubility limit due to the surface and interface energies of nanoparticles. Figure 8b schematically illustrates movement of the boundary between cubic and tetragonal phases during lithiation. With the aid of thermal activation, the boundary generates double kinks in the neighboring tetragonal phase. The kinks then glide apart transversely, and finally the entire boundary advances one periodic lattice. Note that this model assumes very fast Li-ion mobility within the entire material compared to the movement of the boundaries. When one considers long-range elastic interaction between cubic and tetragonal sites due to the elongated Mn−O bond, the additional interaction energy during the movement of the boundary can be expressed as

$$E = \frac{1}{N}\sum_{ij} k_{ij}(u_i - u_j)^2$$

where N is the number of sites, k_{ij} is the elastic interaction between ith and jth sites, and u_i is Mn−O distance of the ith site. The mean field approximation ($k \approx \sum_j k_{ij}$) can transform the interaction energy as

$$E = \Gamma\gamma_b(1 - \gamma_b)$$

where Γ is $2k(u_i - u_j)$,[2] and γ_b is the fraction of the tetragonal site at the boundary. Therefore, the activation energy is

$$E_A = \Gamma(\gamma_{SL} - 0.5)^2$$

where γ_{SL} is the fractional solubility limit for the tetragonal site into the cubic phase. Figure 8b shows the additional elastic interaction energy during the movement of the boundary. The figure clearly indicates that, when the solubility limit is extended due to surface and interface energies, the activation energy for the moving boundaries should be suppressed. This explains the decrease in activation energy with decreasing crystallite size.

However, as shown in Figure 8a, the activation energy for the compound with $L = 15$ nm is 0.25 eV, which is comparable to the typical value for Li-ion diffusion in metal oxides.[53,54] Thus, we should also consider the model where not the moving boundary but rather Li-ion diffusion is a rate-limiting step during lithiation.

Consider now the case where Li-ion diffusion into the spherical $LiMn_2O_4$ is the rate-limiting step, and the moving boundaries disappear. When a potential step is applied to the electrochemical cell at equilibrium, the diffusion equation gives $f(t)$ as,[55]

$$f(t) = 1 - \frac{6}{\pi^2}\sum_{n=1}^{\infty}\frac{1}{n^2}\exp\left(-\frac{n^2\pi^2 D}{d^2}t\right)$$

where D is the chemical Li-ion diffusion coefficient and d is the diffusion length. If t is large enough, $f(t)$ approximates to

$$f(t) = 1 - \frac{6}{\pi^2}\exp\left(-\frac{\pi^2 D}{d^2}t\right)$$

Therefore, when Li-ion diffusion is the rate-limiting step and t is large enough to neglect ln $6/\pi^2$ compared to $(\pi^2 D/d^2)t$, the plot of ln[ln(1/(1 − $f(t)$))] as a function of ln t is also linear with a slope of unity and an intercept that includes the chemical Li-ion diffusion coefficient. Thus, the Arrhenius plot of the intercept can also give the activation energy E_A for Li-ion diffusion. This consideration suggests that a plot obeying the JMA model does not necessarily prove the existence of moving boundaries, and the obtained activation energy should be examined carefully.

For the compound with $L = 15$ nm, the obtained activation energy is comparable to typical values for Li-ion diffusion in metal oxides.[53,54] Considering all experimental results, it is most likely that lithiation of the compound with $L = 15$ nm occurs *via* solid solution state without domain boundaries, which is dominated by Li-ion diffusion with an activation energy of 0.25 eV. Note that this discussion based on the JMA model and the diffusion equation assumes compositional independence of the Li-ion diffusion coefficient and the mov-

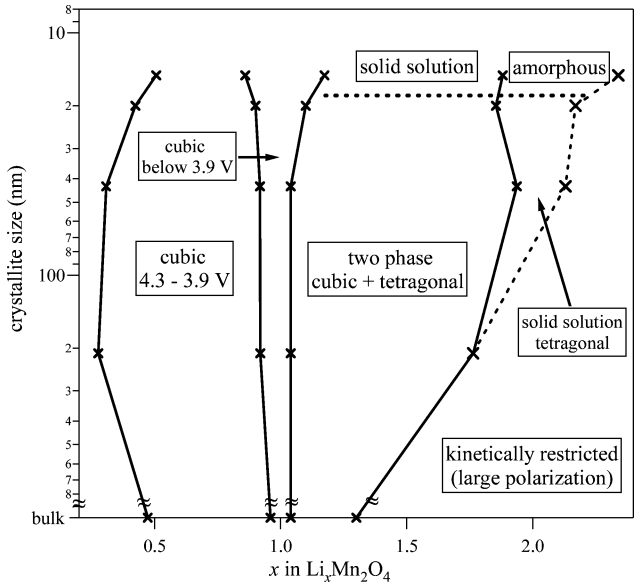

Figure 9. Tentative phase diagram for $Li_xMn_2O_4$ as a function of crystallite size during the lithiation process.

ing speed of the phase boundaries at the first approximation.

Figure 9 shows the phase diagram as a function of crystallite size, summarizing the above discussion. The kinetically restricted composition in the figure corresponds to the region where large polarization is observed during lithiation by the GITT mode. With decreasing crystallite size down to 43 nm, complete lithiation of $Li_{1+x}Mn_2O_4$ clearly becomes possible due to the large surface area, even though domain boundaries between the two phases still exist. Further nanosizing down to 15 nm results in disappearance of the domain boundaries and lithiation without the domain boundaries. The amorphous phase obtained by lithiating the compound with $L = 15$ nm should be closely related to the tetragonal spinel phase from a structural viewpoint, but the Jahn−Teller Mn^{III}-ions may distort, not along the *c*-direction cooperatively, but rather along random directions due to the surface.

Disappearance of the domain boundaries for compounds with $L < 15$ nm means that lithiation is not dominated by the slow moving speed of the domain boundaries. This effect should be important, especially in the high-discharge-rate experiments. To confirm the effect of lithiation without domain boundaries on the high-discharge-rate capability, we performed a high-discharge-rate experiment for nanocrystalline $LiMn_2O_4$.

Figure 10a shows discharge curves for nanocrystalline $LiMn_2O_4$ ($L = 210$, 43, 20, and 15 nm) at various discharge rates from C/4 (74 mA/g) to 10 C (2.96 A/g). Figure 10b shows plots of retained discharge capacity as a function of discharge current density above and below 3.0 V. Above 3.0 V, the capacity at a low current density decreases due to the surface effect. However, with increasing the current density, the capacity for the compounds with large crystallite size rapidly decreases while the capacity for the compounds with small crystallite size is almost constant. This result can be explained by the short Li-ion diffusion length in small particle size. The effect of short Li-ion diffusion length has also been reported for $LiCoO_2$.[12] Concerning the capacity below 3.0 V, the capacity for the compound with $L = 210$ nm abruptly decreases with increasing current density. The capacity at 10 C is only 24% of that at C/4 rate. It is apparent that the decrease in capacity under a high discharge rate is caused by slow movement of the domain boundaries. In contrast, when crystallite size is reduced to 15 nm, capacity improves significantly; for example, the capacity at 10 C is 82% of that at C/4. The improvement below 3.0 V should be ascribed to the fast Li-ion insertion reaction through the

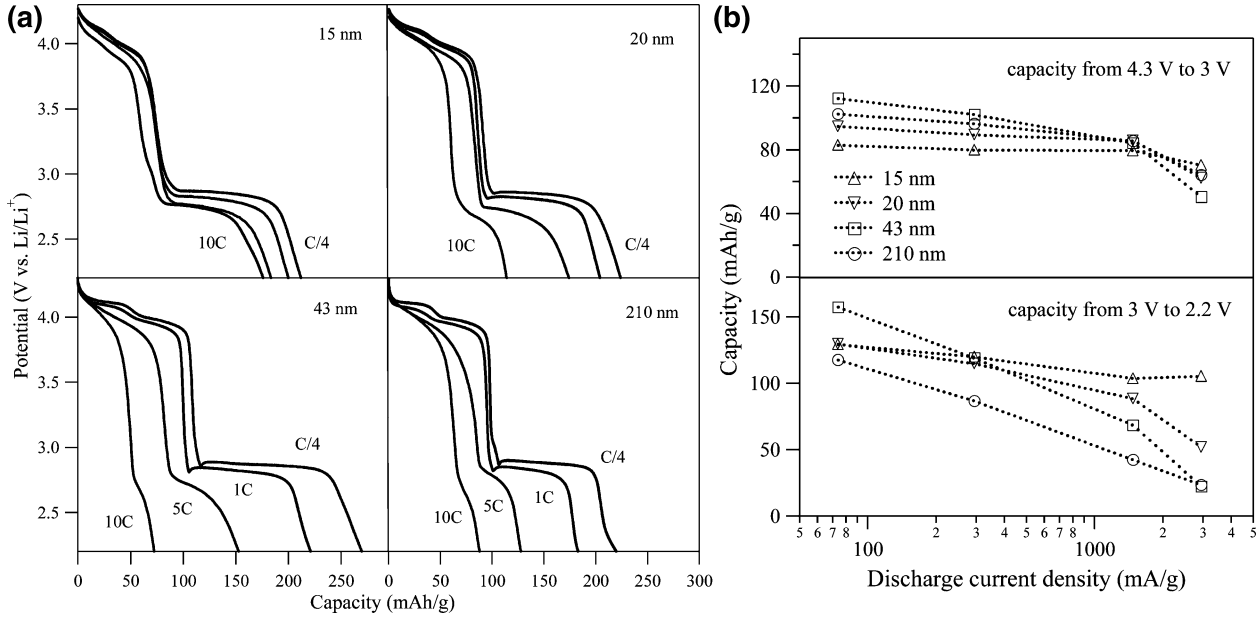

Figure 10. (a) High-discharge-rate curves for nanocrystalline $LiMn_2O_4$, (b) high-discharge-rate capability of nanocrystalline $LiMn_2O_4$.

phase transformation without domain boundaries. By combining two nanosize effects (short Li-ion diffusion length and disappearance of domain boundaries), the high capacity of 180 mAh/g was achieved for nanocrystalline $LiMn_2O_4$ (L = 15 nm) at high current density of 2.98 A/g.

Finally, we address the cyclability of nanocrystalline $LiMn_2O_4$. It is well-known that nanocrystalline electrode materials generally possess poor cyclability due to high reactivity with the electrolyte. Nanocrystalline $LiCoO_2$ is reported to show low cyclability.[12] However, nanocrystalline $LiMn_2O_4$ retains 62% of its initial capacity after 100 cycles (Figure S8, Supporting Information). This cyclability is better than that of bulk $LiMn_2O_4$, which retains only 52% of its initial capacity after 100 cycles. Presumably, lithiation without domain boundaries for nanocrystalline $LiMn_2O_4$ may enable charge/discharge without mechanical stress and hence achieve good cyclability.

CONCLUSIONS

We succeeded in synthesizing nanocrystalline $LiMn_2O_4$ with controlled crystallite size by hydrothermal reaction. The compound's Li-ion deficient stoichiometry becomes more predominant as crystallite size decreases. Electrochemical experiments revealed the large impact of particle size on the Li-ion insertion/extraction reactions. Although large particles cannot be fully lithiated to the tetragonal spinel $Li_2Mn_2O_4$ due to their small surface area, nanoparticles smaller than 43 nm can accommodate a nearly stoichiometric amount of the Li-ion. Nanoparticles smaller than 15 nm show lithiation without domain boundaries, which enables a 10 C discharge rate and good cyclability.

METHODS

All reagents and bulk $LiMn_2O_4$ were purchased commercially. As the precursor for hydrothermal reaction, nanosized orthorhombic $LiMnO_2$ (*o*-$LiMnO_2$) with a nanoplate morphology was synthesized by *in situ* oxidation-ion exchange method.[28] Nanocrystalline $LiMn_2O_4$ was synthesized by hydrothermal reaction. Typically, *o*-$LiMnO_2$ (188 mg, 2 mmol) was stirred in H_2O (30 mL). The colloidal suspension was placed in a stainless steel autoclave and heated to induce hydrothermal reaction. The precipitate was collected by centrifugation, washed with water two times, and dried under vacuum for 12 h to give nanocrystalline $LiMn_2O_4$.

Powder X-ray diffraction (XRD) measurements were performed on an X-ray diffractometer (Bruker D8 Advance) using Cu Kα radiation in steps of 0.008° over the 2θ range 10−80°. Unit cell parameters were calculated by least-squares fitting with peak-top values. TEM measurements were carried out on a JEOL JEM-2100F (200 kV). BET surface area with N_2 adsorption isotherms was measured on a Micromeritrics TriStar 3000. The averaged valence state of Mn-ions was determined according to a procedure reported by Wickham.[36] In this procedure, the nanocrystallline $LiMn_2O_4$ dissolved in a 1.8 N H_2SO_4 aqueous solution containing 7.5×10^{-2} N $VOSO_4 \cdot 3H_2O$ was titrated with a 5×10^{-2} N $KMnO_4$ aqueous solution after addition of concentrated H_3PO_4. The Li/Mn ratio in nanocrystalline $LiMn_2O_4$ was estimated by an inductively coupled plasma atomic emission spectrometer (ICP-AES; RIGAKU CIROS-120). Infrared absorption spectra were obtained on an FT-IR spectrometer (JASCO FT/IR-6200). X-ray absorption spectroscopy (XAS) was performed using a synchrotron X-ray on a beamline BL-9A of High Energy Accelerator Research Organization (Tsukuba), Photon Factory (PF), and the obtained experimental data were analyzed using RIGAKU REX2000.

For electrochemical measurements, each sample (50 mg) was ground with acetylene black (13.3 mg, 20 wt %) and poly(tetrafluoroethylene) (3.33 mg, 5 wt %) into a paste and used. Generally speaking, normal electrodes in commercial Li-ion rechargeable batteries contain only 5 wt % conductive material. However, because we are investigating high rates of Li-ion insertion in nanocrystalline $LiMn_2O_4$, we used 20 wt % conductive material for nanocrystalline $LiMn_2O_4$ as well as bulk $LiMn_2O_4$ to improve electrode conductivity. High conductivity suppresses some unfavorable problems in high-rate experiments, such as IR drop. Li metal was used for the reference and counterelectrodes; $LiClO_4$ EC/DEC solution (1 M) was used for the electrolyte. Regardless of the crystallite size, the cell composition was same for all samples. Cut-off voltages were 4.3 V for charging (extraction of Li-ions) and 2.0 V for discharging (insertion of Li-ions).

Acknowledgment. The authors would thank Ms. A. Fukui and Prof. N. Ishikawa (Osaka University) for the synthesis of nanocrystalline $LiMn_2O_4$. This work was financially supported by the New Energy and Industrial Technology Development Organization, Japan (NEDO). M.O. was financially supported from Grant-in-aid for Scientific research from the Ministry of Education, Culture, Sports, Science and Technology, Japan. M.O. was also financially supported from Tokuyama Science Foundation and Mitsubishi Chemical Corporation Fund.

Supporting Information Available: TEM images, IR spectra, EXAFS spectra, OCV curves, theoretical analysis of nanosize effect on Li-ion insertion above 3 V, energy distribution plots, crystallite-size-dependent plots of averaged OCV and overpotential, cyclability plots, and list of EXAFS-spectrum-fitting parameters.This material is available free of charge *via* the Internet at http://pubs.acs.org.

REFERENCES AND NOTES

1. Armand, M.; Tarascon, J.-M. Building Better Batteries. *Nature* **2008**, *451*, 652–657.
2. Nishide, H.; Oyaizu, K. Materials Science−Toward Flexible Batteries. *Science* **2008**, *319*, 737–738.
3. Kudo, T.; Fueki, K. *Solid State Ionics*; Kodansha: Tokyo, 1990.
4. Guo, Y. G.; Hu, J. S.; Wan, L. J. Nanostructured Materials for Electrochemical Energy Conversion and Storage devices. *Adv. Mater.* **2008**, *20*, 2878–2887.
5. Wang, Y.; Cao, G. Developments in Nanostructured Cathode Materials for High-Performance Lithium-Ion Batteries. *Adv. Mater.* **2008**, *20*, 2251–2269.
6. Maier, J. *Physical Chemistry of Ionic Materials*; John Wiley & Sons Ltd.: England, 2004.
7. Maier, J. Nanoionics: Ion Transport and Electrochemical Storage in Confined Systems. *Nat. Mater.* **2005**, *4*, 805–815.
8. Wagemaker, M.; Borghols, W. J. H.; Mulder, F. M. Large Impact of Particle Size on Insertion Reactions. A Case for Anatase Li_xTiO_2. *J. Am. Chem. Soc.* **2007**, *129*, 4323–4327.
9. Meethong, N.; Huang, H. Y. S.; Speakman, S. A.; Carter, W. C.; Chiang, Y. M. Strain Accommodation during Phase Transformation in Olivine-Based Cathodes as a Materials Selection Criterion for High-Power Rechargeable Batteries. *Adv. Funct. Mater.* **2007**, *17*, 1115–1123.
10. Gibot, P.; Casas-Cabanas, M.; Laffont, L.; Levasseur, S.; Carlach, P.; Hamelet, S.; Tarascon, J. M.; Masquelier, C. Room-Temperature Single-Phase Li Insertion/Extraction in Nanoscale Li_xFePO_4. *Nat. Mater.* **2008**, *7*, 741.
11. Meethong, N.; Kao, Y.-H.; Tang, M.; Huang, H.-Y.; Carter, W.;

Chiang, Y.-M. Electrochemically Induced Phase Transformation in Nanoscale Olivines $Li_{1-x}MPO_4$ (M = Fe, Mn). *Chem. Mater.* **2008**, *20*, 6189–6198.
12. Okubo, M.; Hosono, E.; Kim, J. D.; Enomoto, M.; Kojima, N.; Kudo, T.; Zhou, H. S.; Honma, I. Nanosize Effect on High-Rate Li-Ion Intercalation in $LiCoO_2$ Electrode. *J. Am. Chem. Soc.* **2007**, *23*, 7444–7452.
13. Thackeray, M. M.; David, W. I. F.; Bruce, P. G.; Goodenough, J. B. Lithium Insertion into Manganese Spinels. *Mater. Res. Bull.* **1983**, *18*, 461–472.
14. Liu, W.; Kowal, K.; Farrington, G. C. Mechanism of the Electrochemical Insertion of Lithium into $LiMn_2O_4$ spinels. *J. Electrochem. Soc.* **1998**, *145*, 459–465.
15. Eriksson, T.; Hjelm, A. K.; Lindbergh, G.; Gustafsson, T. Kinetic Study of $LiMn_2O_4$ Cathodes by *in Situ* XRD with Constant-Current Cycling and Potential Stepping. *J. Electrochem. Soc.* **2002**, *149*, A1164–1170.
16. Thackeray, M. M. Manganese Oxides for Lithium Batteries. *Prog. Solid State Chem.* **1997**, *25*, 1–71.
17. Thackeray, M. M. Spinel Electrodes for Lithium Batteries. *J. Am. Ceram. Soc.* **1999**, *82*, 3347–3354.
18. Mishra, S. K.; Ceder, G. Structural Stability of Lithium Manganese Oxides. *Phys. Rev. B* **1999**, *59*, 6120–6130.
19. Chiag, Y. M.; Wang, H.; Jang, Y. I. Electrochemically Induced Cation Disorder and Phase Transformations in Lithium Intercalation Oxides. *Chem. Mater.* **2001**, *13*, 53–63.
20. Mobah, A.; Verbaere, A.; Tournoux, M. Li_xMnO_2—Lambda Phases Related to the Spinel Type. *Mater. Res. Bull.* **1983**, *18*, 1375–1381.
21. Kang, S. H.; Goodenough, J. B. $LiMn_2O_4$ Spinel Cathode Material Showing No Capacity Fading in the 3 V Range. *J. Electrochem. Soc.* **2000**, *147*, 3621–3627.
22. Curtis, C. J.; Wang, J.; Schulz, D. L. Preparation and Characterization of $LiMn_2O_4$ Spinel Nanoparticles as Cathode Materials in Secondary Li Batteries. *J. Electrochem. Soc.* **2004**, *151*, A590–598.
23. Chiu, K. F.; Lin, H. C.; Lin, K. M.; Chen, C. C. Stability Improvement of $LiMn_2O_4$ Thin-Film Cathodes under High-Rate and Over-Discharge Cycling. *J. Electrochem. Soc.* **2006**, *153*, A1992–1997.
24. Kang, S. H.; Goodenough, J. B.; Rabenberg, L. K. Effect of Ball-Milling on 3-V Capacity of Lithium-Manganese Oxospinel Cathodes. *Chem. Mater.* **2001**, *13*, 1758–1764.
25. Jiao, F.; Bao, J.; Hill, A. H.; Bruce, P. G. Synthesis of Ordered Mesoporous Li-Mn-O Spinel as a Positive Electrode for Rechargeable Lithium Batteries. *Angew. Chem., Int. Ed.* **2008**, *47*, 9711–9716.
26. Park, S. H.; Myung, S. T.; Oh, S. W.; Yoon, C. S.; Sun, Y. K. Ultrasonic Spray Pyrolysis of Nanocrystalline Spinel $LiMn_2O_4$ Showing Good Cycling Performance in the 3 V Range. *Electrochim. Acta* **2006**, *51*, 4089–4095.
27. Hosono, E.; Kudo, T.; Honma, I.; Matsuda, H.; Zhou, H. S. Synthesis of Single Crystalline Spinel $LiMn_2O_4$ Nanowires for a Lithium Ion Battery with High Power Density. *Nano Lett.* **2009**, *9*, 1045–1051.
28. Barboux, P.; Tarascon, J.-M.; Shokoohi, F. K. The Use of Acetates As Precursors for the Low-Temperature Synthesis of $LiMn_2O_4$ and $LiCoO_2$ Intercalation Compounds. *J. Solid State Chem.* **1991**, *94*, 185–196.
29. Lines, M. E.; Glass, A. M. *Principles and Applications of Ferroelectrics and Related Materials*; Clarendon: Oxford, U.K., 1977.
30. Frey, M. H.; Payne, D. A. Grain-Size Effect on Structure and Phase Transformations for Barium Titanate. *Phys. Rev. B* **1996**, *54*, 3158–3168.
31. Ozuku, T.; Ueda, A.; Hirai, T. *Chem. Express* **1992**, *7*, 193.
32. Li, X. D.; Yang, W. S.; Zhang, S. C.; Evans, D. G.; Duan, X. The Synthesis and Characterization of Nanosized Orthorhombic $LiMnO_2$ by *in Situ* Oxidation-Ion Exchange. *Solid State Ionics* **2005**, *176*, 803–811.
33. Yonemura, M.; Yamada, A.; Kobayashi, H.; Tabuchi, M.; Kamiyama, T.; Kawamoto, Y.; Kanno, R. Synthesis, Structure, and Phase Relationship in Lithium Manganese Oxide Spinel. *J. Mater. Chem.* **2004**, *14*, 1948–1958.
34. Schimmel, H. G.; Montfrooij, W.; Kearley, G. J.; Verhoeven, V. W. J.; de Schepper, I. M. Neutron Scattering Investigation of the Spin Dynamics in $Li[Mn_{1.94}Li_{0.04}]O_{3.94}$. *Phys. Rev. B* **2001**, *63*, 214409.
35. Kanno, R.; Kondo, A.; Yonemura, M.; Gover, R.; Kawamoto, Y.; Tabuchi, M.; Kamiyama, T.; Izumi, F.; Masquelier, C.; Rousse, G. The Relationships between Phases and Structures of Lithium Manganese Spinels. *J. Power Sources* **1999**, *81−82*, 542–546.
36. Ammundsen, B.; Jones, D. J.; Rozire, J.; Burns, G. R. Effect of Chemical Extraction of Lithium on the Local Structure of Spinel Lithium Manganese Oxides Determined by X-ray Absorption Spectroscopy. *Chem. Mater.* **1996**, *8*, 2799–2808.
37. Aitchson, P.; Ammundsen, B.; Jones, D. J.; Burns, G.; Roziere, J. Cobalt Substitution in Lithium Manganate Spinels: Examination of Local Structure and Lithium Extraction by XAFS. *J. Mater. Chem.* **1999**, *9*, 3125–3130.
38. Strobel, P.; Darie, C.; Thiery, F.; Ibarra-Palos, A.; Bacia, M.; Proux, O.; Soupart, J. B. Electrochemical Lithium Intercalation in Nanosized Manganese Oxides. *J. Phys. Chem. Solids* **2006**, *67*, 1258–1264.
39. Wickham, D. G.; Whipple, E. R. *Talanta* **1963**, *10*, 314.
40. Feng, Q.; Miyai, Y.; Kanoh, H.; Ooi, K. Li^+ Extraction/Insertion with Spinel-Type Lithium Manganese Oxides—Characterization of Redox-Type and Ion-Exchange-Type Sites. *Langmuir* **1992**, *8*, 1861–1867.
41. Fang, C. M.; de Wijs, G. A.; Loong, C. K.; de With, G. Lattice and Local-Mode Vibrations in Anhydrous and Protonized $LiMn_2O_4$ Spinels from First-Principles Theory. *J. Mater. Chem.* **2007**, *17*, 4908–4913.
42. Bruce, P. G. *Solid State Electrochemistry*; Cambridge University Press: Cambridge, U.K., 1995.
43. Kudo, T.; Hibino, M. Consideration on the Potential-Composition Relationships Observed with Amorphous Intercalation Systems such as Li_xWO_3. *Solid State Ionics* **1996**, *84*, 65–72.
44. Kudo, T.; Hibino, M. Theoretical Dependence of the Free Energy and Chemical Potential upon Composition in Intercalation Systems with Repulsive Interaction between Guest Ions. *Electrochim. Acta* **1998**, *43*, 781–789.
45. Okubo, M.; Kim, J. D.; Kudo, T.; Zhou, H. S.; Honma, I. Anisotropic Surface Effect on Electronic Structures and Electrochemical Properties of $LiCoO_2$. *J. Phys. Chem. C* **2009**, *113*, 15337–15342.
46. Jamnik, J.; Maier, J. Nanocrystallinity Effects in Lithium Battery Materials—Aspects of Nano-ionics. Part IV. *Phys. Chem. Chem. Phys.* **2003**, *5*, 5215–5220.
47. Wagemaker, M.; Mulder, F. M.; Van der Ven, A. The Role of Surface and Interface Energy on Phase Stability of Nanosized Insertion Compounds. *Ad. Mater.* **2009**, *21*, 2703.
48. Johnson, A. M.; Mehl, R. F. Reaction Kinetics in Processes of Nucleation and Growth. *Trans. Am. Inst. Mining Met. Eng.* **1939**, *135*, 416–442.
49. Avrami, M. Kinetic of Phase Change I. *J. Chem. Phys.* **1939**, *7*, 1103.
50. Avrami, M. Kinetic of Phase Change II. *J. Chem. Phys.* **1940**, *8*, 212.
51. Avrami, M. Kinetic of Phase Change III. *J. Chem. Phys.* **1941**, *9*, 177.
52. Allen, J. L.; Jow, T. R.; Wolfenstine, J. Kinetic Study of the Electrochemical $FePO_4$ to $LiFePO_4$ Phase Transition. *Chem. Mater.* **2007**, *19*, 2108–2111.
53. Okubo, M.; Tanaka, Y.; Zhou, H. S.; Kudo, T.; Honma, I. Determination of Activation Energy for Li-Ion Diffusion in Electrodes. *J. Phys. Chem. B* **2009**, *113*, 2840.
54. Kang, K.; Meng, Y. S.; Breger, J.; Grey, C. P.; Ceder, G. Electrodes with High Power and High Capacity for Rechargeable Lithium Batteries. *Science* **2006**, *311*, 977–980.
55. Crank, J. C. *Mathematics of Diffusion,* 2nd ed.; Oxford University Press: Oxford, U.K., 1975.